ARTICLE

Check for updates

A solution to the complement of the generalized Luneburg lens problem

Nelson J. G. Fonseca [1✉], Tomáš Tyc[2] & Oscar Quevedo–Teruel [3]

Lenses are of interest for the design of directive antennas and multi-optics instruments in the microwave, terahertz and optical domains. Here, we introduce an optical problem defined as the complement of the well-known generalized Luneburg lens problem. The spherically symmetric inhomogeneous lenses obtained as solutions of this problem transform a given sphere in the homogeneous region outside of the lens into a virtual conjugate sphere, forming a virtual image from a real source. An analytical solution is proposed for the equivalent geodesic lens using the analogy between classical mechanics and geometrical optics. The refractive index profile of the corresponding inhomogeneous lens is then obtained using transformation optics. The focusing properties of this family of lenses are validated using ray-tracing models, further corroborated with full-wave simulations. The numerical results agree well with the predictions over the analyzed frequency bandwidth (10–30 GHz). This virtual focusing property may further benefit from recent developments in the fields of metamaterials and transformation optics.

[1] Antenna and Sub-Millimetre Waves Section, European Space Agency, 2200 AG Noordwijk, Noordwijk, The Netherlands. [2] Institute of Theoretical Physics and Astrophysics, Faculty of Science, Masaryk University, Kotlářská 2, 61137 Brno, Czech Republic. [3] School of Electrical Engineering and Computer Science, KTH Royal Institute of Technology, SE-100 44 Stockholm, Sweden. ✉email: nelson.fonseca@esa.int

The so-called generalized Luneburg lens problem was first formulated in its simplest form in the 1853 Cambridge and Dublin Mathematical Journal[1], describing a "transparent medium [...] such that a ray of light within it is a given circle, the index of refraction being a function of the distance from a given point in the plane of the circle". The mathematical solution to that specific problem was published in the 1854 edition of the same journal[2]. An interesting feature of the described "transparent medium" is that "all the rays proceeding from any point in the medium will meet accurately in another point", a characteristic of absolute optical instruments, with no aberrations[3–6]. Although published anonymously, the problem and its solution are attributed to Maxwell[7] and the corresponding medium occupying the entire space was called *Maxwell's fish-eye*[3]. In the engineering community, the bounded version of this medium that is truncated at the normalized radius found more interest and is now generally called *Maxwell's fish-eye lens*. This latter design is a particular case of the more general problem formulated about a century later by Luneburg[8] where each point of a given sphere has a perfect image on another concentric sphere, the object and its image being in an homogeneous region outside or on the surface of the spherically symmetric inhomogeneous lens. For the particular case of Maxwell's fish-eye lens, both of the conjugate spheres are on the surface of the lens. In the case of the so-called Luneburg lens[8], one sphere is on the surface of the lens and the conjugate sphere is at infinity, corresponding to the perfect collimation of a spherical wave emerging from a point source.

The definition of this problem was later extended by Eaton to include the possibility of having one of the spheres inside of the lens and to also have a point source and its image not aligned with the center of the lens[9]. A particular solution to this generalized problem is called the Eaton lens and works as an omnidirectional retro-reflector. Another particular case of interest is the Gutman lens[10], which behaves as a Luneburg lens with its focal surface (or focal arc in the case of a planar implementation) inside the lens. Morgan extended that particular case by proposing a more general formulation of the Luneburg lens problem, which includes also the possibility of having one sphere inside the lens and the other outside the lens[11]. The formulation of the problem being reciprocal, the sphere inside the lens may correspond to either the source or the image. Besides the few specific cases mentioned above, the generalized Luneburg lens problem has no simple closed-form expression. Various methods had been proposed to solve the problem numerically, with residual aberrations depending on the achieved numerical accuracy[11–13].

An equivalent to the planar Luneburg lens with a constant refractive index was proposed by Rinehart[14,15] and is known in its general form as the geodesic lens. The Rinehart–Luneburg lens has a simple closed-form expression when its rotationally symmetric profile is defined using the arc length measured from the symmetry axis as a function of the lens radius. This equivalence may be seen as an early implementation of conformal mapping, or transformation optics (TO)[16,17], with Kunz[18] extending the particular transformation described by Rinehart to a more general equivalence between two rotationally symmetric surfaces. This property was recently exploited by Šarbort and Tyc[19] to provide a solution to the generalized Luneburg lens problem by deriving the analytical expression of its equivalent geodesic lens problem.

All the lenses discussed above are designed to produce a real image as a direct consequence of the formulation of the generalized Luneburg lens problem (see Fig. 1a). Miñano[4] noticed that an Eaton lens forms a virtual image diametrically opposite to the point source, corresponding to an absolute instrument with negative unit magnification. A similar property was obtained with the magnifying absolute instruments based on Eaton and Luneburg lenses described in[20]. Another class of spherically symmetric lenses providing virtual images is the so-called invisible lens, which produces an image collocated with the source, corresponding to a positive unit magnification[4,21,22]. Some less conventional geodesic and nonuniform refractive lenses were discussed in[23] to produce optical components equivalent to well-known microwave components for use in microwave and optical circuitry. However, none of the spherically symmetric lenses reported above provide the more general transformation of a given sphere into a virtual conjugate sphere (see Fig. 1b). This problem is introduced here as the complement of the generalized Luneburg lens problem and is solved using the approach described in[19]. An analytical solution is also provided for its equivalent geodesic lens. This analytical formula can be used to evaluate the refractive index profile of any spherically and rotationally symmetric lens with the described virtual image property.

The Luneburg lens and its derivatives received a lot of attention since their inception because they provide unique scanning properties and require materials with relatively low refractive index, easy to engineer from existing materials. Early applications were mostly radar systems steering a highly directive beam over a wide angular range (up to full azimuthal coverage in some cases)[10,15,24,25]. With recent developments on metamaterials and TO[26–30], there have been several advances reported in the microwave, terahertz, and optical domains[31–36], with applications in terrestrial communications, satellite communications, and automotive radars to name a few[37–41]. Spherically and rotationally symmetric lenses producing sharp virtual images may be of interest in multi-optics systems, extending the range of existing solutions. They could be used in combination with reflector systems, improving for example the unifocal property of the hyperbolic sub-reflector in a classical dual-reflector Cassegrain geometry[42]. A unifocal lens with a virtual focal point was implemented in a dual-transmitarray configuration to reduce the overall height of the antenna system[43]. A similar unifocal dual-lens system based on homogeneous lenses is described in[44].
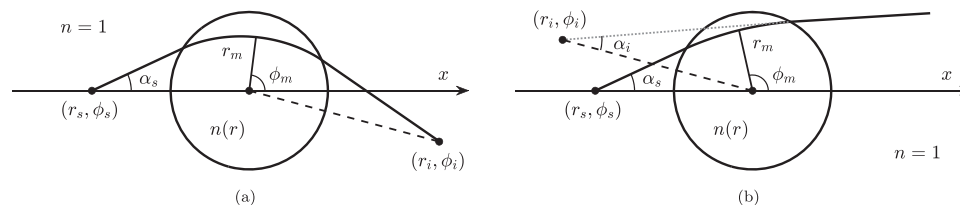

Fig. 1 Spherically symmetric inhomogeneous lens problems. A schematic representation of (**a**) the generalized Luneburg lens problem and (**b**) the proposed complementary problem is provided to define all design parameters. The circles delimit the boundaries between the inhomogeneous medium, $n(r)$, and the homogeneous medium, $n = 1$. The inhomogeneous profile is such that any ray emerging from the source, represented by the point of coordinates (r_s, ϕ_s) and hitting the lens, passes through a point image of coordinates (r_i, ϕ_i) on the focal axis represented by dashed lines. In the case of the proposed complementary problem, it is as if the ray would emerge from the virtual image in a homogeneous medium, hence the partial representation of the ray in dotted line.

However, the extension of these specific solutions to the spherically and rotationally symmetric lenses described here is not straightforward. In its planar form, the general lens solution introduced in this paper could be combined with the doubly curved reflector geometry proposed in[45].

This paper describes first the general problem, introduced as the complement of the generalized Luneburg lens problem. An analytical solution to the equivalent geodesic lens problem is derived, enabling the evaluation of different variations of the proposed lens supported by numerical results. An extension of the proposed general lens solution combined with simple mirrors is also discussed. Numerical results are provided to validate the proposed solution. Finally, some conclusions are drawn and perspectives are discussed.

Results and discussion

Problem formulation. The problem, as formulated by Luneburg himself, is to find a spherically symmetric partly inhomogeneous medium, corresponding to the desired lens, "such that two given spheres in the homogeneous part are perfect conjugate spheres"[8]. Including the extension formulated by Eaton, who suggested to remove "the restriction imposed by Luneburg that the emerging rays be parallel to the axis of symmetry of the system"[9] for the particular case of a conjugate sphere at infinity, one can schematically represent the problem to be solved with Fig. 1a. The spherical symmetry of this problem enables us to reduce its study to any plane passing through the center of the lens. Thus, it is convenient to use the polar coordinates (r, ϕ). The problem can also be normalized to the radius of the lens without loss of generality. A refractive index of 1 is assumed in the homogeneous region outside of the lens, here also without loss of generality as the problem may be scaled by any desired value. Note that the problem is described assuming a direction of propagation. However, the rays propagating in the forward direction could equally propagate in the backward direction, as a direct implication of the Stoke-Helmholtz reciprocity principle. Thus, no specific direction of propagation is highlighted in the ray-tracing representations provided here to emphasize that the source and the image may be swapped.

The problem is then to define the refractive index of the lens as a function of the radial coordinate, $n(r)$, such that any ray emerging from a point source, at location (r_s, ϕ_s), and hitting the lens, passes through a point image at location (r_i, ϕ_i). As a consequence of the rotational symmetry, a distributed source on the sphere with radius r_s produces a distributed image on the conjugate sphere with radius r_i having a magnification of r_i/r_s. This property derives from the triangle similarity theorems. Note that with the generalization proposed by Eaton[9], the image of a point source is in fact a circle with axis of symmetry the x-axis and radius $r_i \sin \phi_i$. This lens produces a conical wavefront in the particular case of a conjugate sphere at infinity. The image circle reduces to a point image when $\phi_i - \phi_s = 0[\pi]$. The time to travel from the object to its image, or in other words the optical path length of the ray trajectory between the object and its image, is independent of the angular direction at the origin, α_s. A convenient way to formulate and solve the problem is to consider the inverse problem, which consists in finding the ray trajectory assuming the refractive index, $n(r)$, is known, and to make use of the well-known analogy between classical mechanics and geometrical optics. One may refer to[19] for a detailed derivation of the equations in the case of the generalized Luneburg lens problem and for the analytical expression of the corresponding equivalent geodesic lens.

Here a different problem is introduced. The problem remains to find a spherically symmetric medium such that two given

spheres in the homogeneous part are perfect conjugate spheres. However, the problem is formulated such that the image is always virtual, as represented in Fig. 1b. The rays emerging from the lens are seen as if emerging from a point image (r_i, ϕ_i) rather than converging to it. Equivalent parameter values are used in Fig. 1 to represent the two problems in order to emphasize their complementary nature. While the generalized Luneburg lens problem defines lenses focusing on one half of the focal axis (represented with dashed lines in Fig. 1), the reformulated problem defines lenses focusing on the complementary half of that focal axis. The complementary nature of the two problems is further highlighted through the specific examples discussed here. Because the proposed complementary problem maintains rotational symmetry, the magnification of the proposed lenses is also r_i/r_s.

Using the analogy between classical mechanics and geometrical optics, a ray trajectory is characterized by a constant value of the quantity L, labeled as an angular momentum in reference to its classical mechanics counterpart, and given by:

$$L = rn(r)\sin\alpha, \tag{1}$$

where α is defined here as the angle measured towards the origin between the radial vector and the local tangent to the ray at any given point. Note that in some works, the supplementary angle is used instead, which does not change the value of L. This angle is represented in Fig. 1b for the particular cases of the point source and the point image with values α_s and α_i, respectively. This enables to evaluate L as a function of these angles and the radial position of the point source or point image as follows:

$$L = r_s \sin\alpha_s = r_i \sin\alpha_i. \tag{2}$$

There is another particular point of interest, also illustrated in Fig. 1, for which the ray trajectory has a minimum radius, r_m. At this particular point, $\alpha = \pm\pi/2$.

To simplify the analytical expressions, Luneburg[8] introduced the radial quantity $\rho = rn(r)$, referred to as the turning parameter in recent literature[21]. This quantity corresponds to the radial coordinate transformation between a planar rotationally symmetric inhomogeneous lens and its geodesic equivalent[14,18]. Using differential geometry, the elementary angular displacement of a ray in a spherical medium with refractive index $n(r)$ is given by:

$$d\phi = \pm \frac{Ldr}{r\sqrt{\rho^2 - L^2}}. \tag{3}$$

In ref. [19], the parameter M is introduced to quantify the total change of polar angle as the ray propagates from the source to the image such that $\phi_i - \phi_s = -M\pi$, where M is a non-negative real number. Note that in the case of the nominal Luneburg lens problem[8], where any point source and associated point image are aligned with the center of the lens, $M = 1$. In the proposed reformulated problem, the corresponding nominal case, where the point source, the point image, and the lens center are aligned, is obtained for $M = 0$. Using the same notation and counting the virtual portion of the ray trajectory negatively, the following equation is derived for the proposed complementary problem:

$$-M\pi = \int_{r_s}^1 \frac{Ldr}{r\sqrt{r^2 - L^2}} - 2\int_{r_m}^1 \frac{Ldr}{r\sqrt{\rho^2 - L^2}} \\ - \int_{r_i}^1 \frac{Ldr}{r\sqrt{r^2 - L^2}}. \tag{4}$$

The first and second terms on the right-hand side of the equation correspond to the real ray trajectory, these terms corresponding to the propagation outside the lens and inside the lens, respectively. The third term corresponds to the virtual propagation from the point image, and is the term counted negatively compared to the same equation in[19]. This leads to the

following implicit equation, which defines r as a function of ρ:

$$\int_{r_m}^{1} \frac{L\mathrm{d}r}{r\sqrt{\rho^2 - L^2}} = \frac{1}{2}\left(M\pi + \arcsin\frac{L}{r_s} - \arcsin\frac{L}{r_i}\right). \quad (5)$$

The quantity between brackets on the right-hand side is the scattering angle, χ, defined as the angular change to the ray trajectory in the homogeneous medium before and after the lens and counted positively when the ray is bent towards the x-axis. With this quantity, defined as a function of L, one can find the refractive index using the formula described in[8]:

$$n = \frac{\rho}{r} = \exp\left(\frac{1}{\pi}\int_{\rho}^{1}\frac{\chi(t)\mathrm{d}t}{\sqrt{t^2 - \rho^2}}\right) \quad (6)$$

This formulation is based on a variation of the inverse Radon Transform introduced by Luneburg[8], where the integration range is reduced to part of the lens region. Equation (6) provides the general solution to the proposed problem in the form $(n(\rho), r(\rho))$, defining the radial distribution of the refractive index of the lens, $n(r)$, as a parametric function of ρ which may be solved numerically in the general case. In fact, Eq. (6) can be found directly from geometrical considerations giving the scattering angle, $\chi(L)$. However, the derivation leading to Eq. (5) is of interest as it helps defining an analytical formula for the proposed family of lenses using the equivalence with geodesic lenses, following an approach similar to the one described in[19]. A more general equivalence between two rotationally symmetric lenses on curved surfaces has been described[18,46]. For the purposes of this work, it is sufficient to consider the equivalence between a planar inhomogeneous lens and a homogeneous geodesic lens.

Before discussing the equivalent geodesic lens problem, one can already make some general remarks on the solutions to the complement of the generalized Luneburg lens problem formulated here. For the particular case $\chi = 0$, Eq. (6) leads to $n = 1$, which is the trivial invisible lens solution. Another important remark, for the nominal case where $M = 0$, is that the sign of the scattering angle χ is independent of L and is positive when $r_i \geq r_s$. This sign determines the sign of the integral in Eq. (6), meaning that the resulting refractive index is such that $n(r) \geq 1, \forall\, r \in [0, 1]$, when $r_i \geq r_s$. This property is true for any relative position of the source and its image in the case of the generalized Luneburg lens problem, as the scattering angle is always positive (see Fig. 1a). With the proposed lens, the scattering angle is negative for $r_i < r_s$ and $M = 0$. This specific configuration results in a refractive index $n(r) \leq 1, \forall\, r \in [0, 1]$, thus requiring to either adapt the refractive index of the homogeneous region outside the lens or to use adequate metamaterials. This opens opportunities for interesting developments.

Equivalent geodesic lens. The equivalence between a rotationally symmetry inhomogeneous lens and a geodesic lens is used to find an analytical solution to the proposed complementary problem[19]. The transformation, or conformal mapping, between the two lenses is defined by[14,18]:

$$\begin{cases} \rho = nr \\ \mathrm{d}s = n\mathrm{d}r \end{cases} \quad (7)$$

where $s(\rho)$ is the arc length measured from the axis of symmetry of a rotationally symmetric geodesic lens defined in the cylindrical coordinate system (ρ, θ, z), as represented in Fig. 2. With this coordinate transformation, Eq. (3) becomes

$$\mathrm{d}\theta = \pm\frac{Ls'(\rho)\mathrm{d}\rho}{\rho\sqrt{\rho^2 - L^2}}, \quad (8)$$

where $L = \rho\sin\alpha$, with α being defined here as the angle between
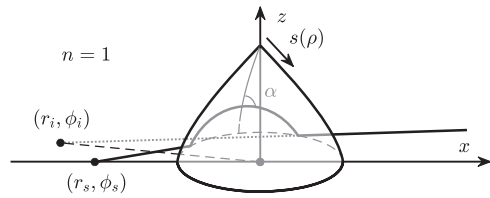

Fig. 2 Equivalent geodesic lens problem. Schematic representation of the trajectory of a ray emerging from the point source of cylindrical coordinates (r_s, ϕ_s) and propagating in the equivalent geodesic lens, coming out of the lens as if emerging from the virtual point image of coordinates (r_i, ϕ_i), where the angle ϕ is defined with respect to the x-axis. The ray is represented in light gray when passing behind the geodesic lens surface, with the actual ray trajectory in solid line and the virtual one in dotted line. The medium of propagation is homogeneous and normalized, $n = 1$.

the ray trajectory and the meridian in the lens (see Fig. 2), and $s'(\rho) = \mathrm{d}s/\mathrm{d}\rho$. This leads to the following implicit expression of the derivative of $s(\rho)$, equivalent to Eq. (5):

$$\int_{L}^{1}\frac{Ls'(\rho)\mathrm{d}\rho}{\rho\sqrt{\rho^2 - L^2}} = \frac{1}{2}\left(M\pi + \arcsin\frac{L}{r_s} - \arcsin\frac{L}{r_i}\right). \quad (9)$$

This equation differs from the one of the generalized Luneburg lens problem[19] in that the term with r_i is negative. Thus, all terms that come from $\arcsin(L/r_i)$ in[19] have to be taken with a negative sign. The term that comes from the generalization of the problem, $M\pi/2$, and which replaces $M\pi/2 - \arcsin(L)$ in[19], needs to be reevaluated. The derivation of the associated term is detailed in the Methods and illustrates the use of Abel's integral equation to solve this problem. With these considerations, one can derive the following closed-form expression for the general equivalent geodesic lens solution to the proposed problem:

$$\begin{aligned} s(\rho) = \rho - \frac{1}{\pi}&\left[\rho\arcsin\sqrt{\frac{1-\rho^2}{r_s^2 - \rho^2}} - \rho\arcsin\sqrt{\frac{1-\rho^2}{r_i^2 - \rho^2}}\right.\\ &+ r_s\arcsin\left(\rho\sqrt{\frac{r_s^2 - 1}{r_s^2 - \rho^2}}\right) - r_i\arcsin\left(\rho\sqrt{\frac{r_i^2 - 1}{r_i^2 - \rho^2}}\right)\\ &+ \left.\left(\sqrt{r_i^2 - 1} - \sqrt{r_s^2 - 1} + \arcsin\frac{1}{r_i} - \arcsin\frac{1}{r_s}\right)\arcsin\rho\right]\\ &+ M\arcsin\rho\,. \end{aligned}$$

$$(10)$$

Assuming $r_s = 1$ and $M = 0$, this expression reduces to:

$$s(\rho) = \frac{\rho}{2} + \frac{1}{\pi}\left[\rho\arcsin\sqrt{\frac{1-\rho^2}{r_i^2 - \rho^2}} + r_i\arcsin\left(\rho\sqrt{\frac{r_i^2 - 1}{r_i^2 - \rho^2}}\right)\right.\\ \left. - \left(\sqrt{r_i^2 - 1} + \arcsin\frac{1}{r_i} - \frac{\pi}{2}\right)\arcsin\rho\right].$$

$$(11)$$

The corresponding geodesic lens profile in cylindrical coordinates (ρ, θ, z) is obtained from the differential equation $dz^2 = ds^2 - d\rho^2$, while the inhomogeneous lens refractive index profile, $n(r)$, is obtained from the coordinate transformation defined by Eq. (7). The following subsections provide numerical results, comparing the generalized Luneburg lens problem and the proposed complementary problem.

Discussion on complementarity. Numerical results are provided first to emphasize the complementarity of the two problems discussed above. The geodesic lens profiles are obtained using Eq.
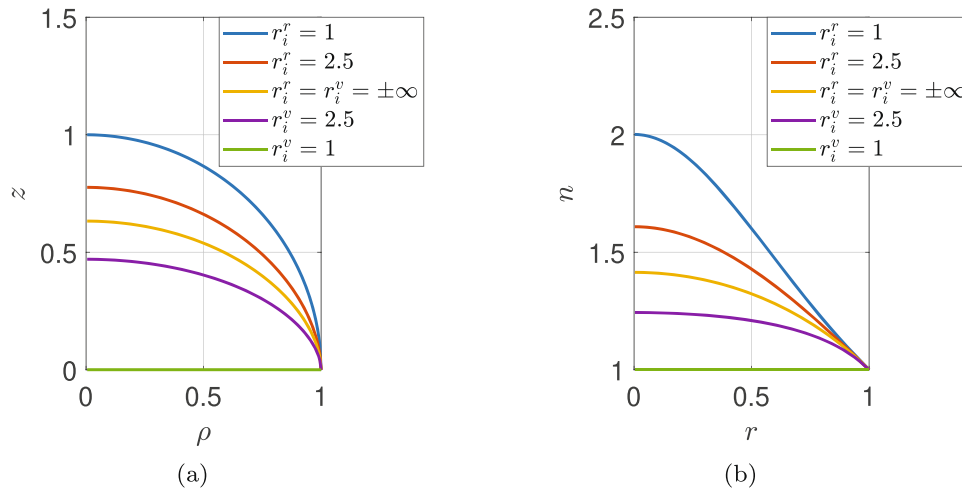
Fig. 3 Comparison of the generalized Luneburg lenses with the proposed complementary lenses. Numerical results are provided for various image radii r_i corresponding to (a) geodesic lens profile height z as a function of the radial coordinate ρ and (b) inhomogeneous lens refractive index n as a function of the radial coordinate r. Solutions to the generalized Luneburg lens problem are marked with a superscript "r", for real image, while solutions to the complementary problem proposed are marked with a superscript "v", for virtual image. Geometrical parameters are all normalized to the lens radius. In all cases, the point source is on the surface of the lens, at radial distance $r_s = 1$, and the source, image and lens center are aligned. The yellow lines correspond to the reference Luneburg lens solution, which is a common solution of the two problems with a real image at $+\infty$ and a virtual image at $-\infty$ on the focal axis.

(10), while the inhomogeneous lens profiles are evaluated numerically from the equivalence defined by Eq. (7). Numerical results for the generalized Luneburg lens problem are obtained using corresponding formulas in[19]. The comparison of the geodesic lens profiles and inhomogeneous lens profiles are provided in Fig. 3 for the case $r_s = 1$, corresponding to a source on the surface of the lens, and different values of the image radius, $r_i \geq 1$. A distinction is made using superscripts, with r_i^r corresponding to a real image lens design while r_i^v refers to a virtual image lens solution as proposed in this paper. The conventional Luneburg lens, corresponding to an image at infinity, is a common solution to both problems. In the case of the generalized Luneburg lens problem, the real image is located at $+\infty$, while in the case of the proposed complementary problem, the virtual image is at $-\infty$. This common solution corresponds to the yellow lines in Fig. 3. The generalized Luneburg lens problem covers the space between those curves and the ones of Maxwell's fish-eye lens, with an image on the surface of the lens and corresponding to the blue lines in Fig. 3. An example of intermediate lens design is provided for $r_i^r = 2.5$ (orange lines). The profiles of the solutions with a real image inside of the lens[11] cover the space above Maxwell's fish-eye lens in Fig. 3.

The solutions to the proposed complementary problem occupy the space between the standard Luneburg lens and the trivial invisible lens solution, corresponding to a flat geodesic lens or an inhomogeneous lens with uniform refractive index equal to 1, both represented with green lines in Fig. 3. An example of intermediate lens design is provided for $r_i^v = 2.5$ (purple lines). These results provide a good visualization of the complementary nature of the two problems. The proposed lens family leads to geodesic lens profiles lower than those of the generalized Luneburg lens problem, or similarly, lower refractive index profiles, which is expected to facilitate practical implementations and integration. As already observed in the subsection "Problem formulation", a virtual image inside of the lens would lead to solutions below the invisible lens case, $r_i = r_s$. This may be achieved in the case of inhomogeneous lenses with a refractive index below 1, using engineered materials. However, this is not achievable with geodesic lenses, as profiles with negative height

values are in fact just symmetric designs of those with positive height values. This follows from the condition $ds \geq d\rho$ which expresses the obvious fact that an elementary arc length, ds, cannot be shorter than the corresponding elementary radial displacement, $d\rho$, in a geodesic lens. When combined with Eq. 7, this leads to the condition $dn/dr \leq 0$ in the equivalent inhomogeneous lens. Thus, $n(r)$ is a monotonically decreasing function that is always greater or equal to its value at the periphery of the lens and $n(r) \geq 1, \forall r \in [0, 1]$, with the normalized notations used in this paper. The symmetric property of $z(\rho)$ with respect to any plane perpendicular to the z-axis was exploited by Kunz[18] to fold the conventional geodesic lens, and was revisited recently to design low-profile geodesic lenses[39–41]. In particular, the numerical results reported in[40] confirm that the refractive index in the inhomogeneous lens equivalent to a modulated geodesic lens remains a monotonically decreasing function. Although the geodesic equivalent does not exist for inhomogeneous lenses with $n(r) \leq 1, \forall r \in [0, 1]$, corresponding to the configuration with a virtual image closer to the lens center than the source, $r_i < r_s$, Eq. 10 still provides a numerical result that can be used to determine the refractive index, $n(r)$, for that particular case, as demonstrated in the following subsection.

Ray-tracing models. Using the ray-tracing tool developed in[40] to analyze modulated geodesic lenses based on the non-Euclidian transformation of Eq. (7), some further numerical results are provided in this section exploring various configurations of the proposed family of lenses. The virtual image lens reported in Fig. 4a corresponds to the intermediate case also illustrated in Fig. 3 with $r_s = 1$ and $r_i = 2.5$. The rays have all the same length. A portion of an arc centered on the virtual image is illustrated with a red line in the case of the inhomogeneous lens, confirming the desired property. A ray-tracing representation of the equivalent geodesic lens is also provided in Fig. 4c. A second lens configuration is illustrated in Fig. 4b for the case of a source away from the lens, $r_s = 1.5$, while keeping the virtual image at the same position, $r_i = 2.5$. Moving the real source away from the lens and towards the virtual image reduces the maximum refractive index and corresponding height of the geodesic lens, as expected (see
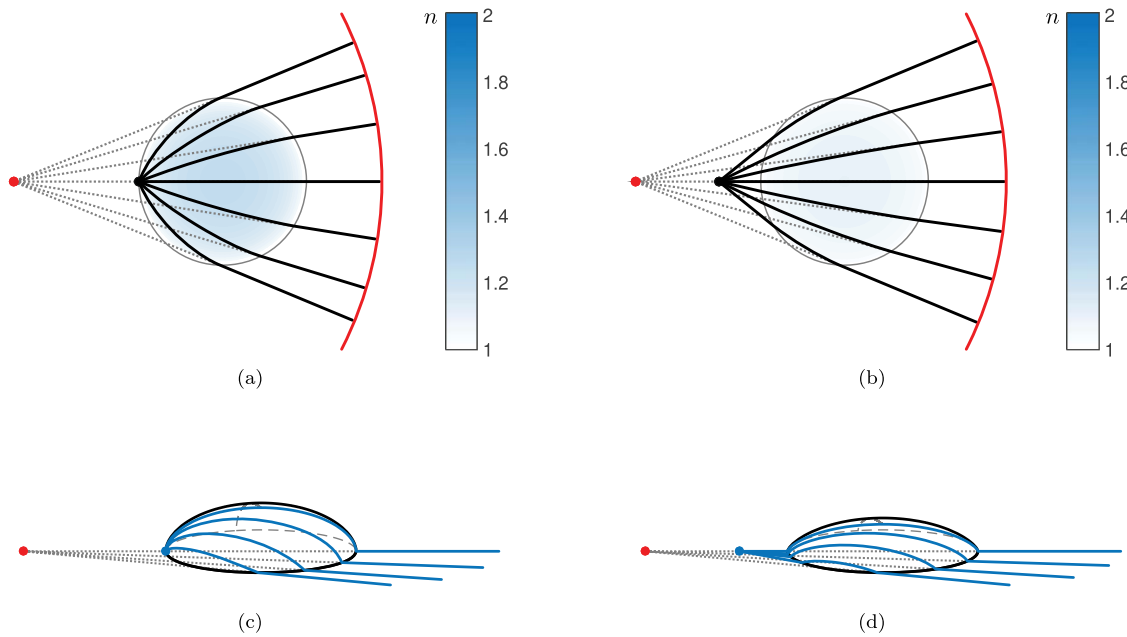
Fig. 4 Virtual image lenses with a source closer to the lens than the image. A ray-tracing representation is provided in the case $r_s < r_i$, with the actual rays in solid lines and the virtual rays in dotted lines. **a**, **b** Inhomogeneous and (**c**, **d**) geodesic lenses are compared for two source positions: (**a**, **c**) $r_s = 1$ and (**b**, **d**) $r_s = 1.5$, with $r_i = 2.5$ and $M = 0$ in both cases, where M is a parameter proportional to the total change of polar angle as the ray propagates from the source to the image. Here, the source, the image and the center of the lens are aligned. All dimensions are normalized to the lens radius. The point source and emerging rays are illustrated in black in the case of inhomogeneous lenses and in blue in the case of geodesic lenses. The virtual image is represented in both cases with a red dot. The expected wavefront is illustrated with a red arc in the case of the inhomogeneous lenses. All rays are represented with the same electrical length, with the end of the rays marking an equiphase front, in agreement with the expected wavefront.
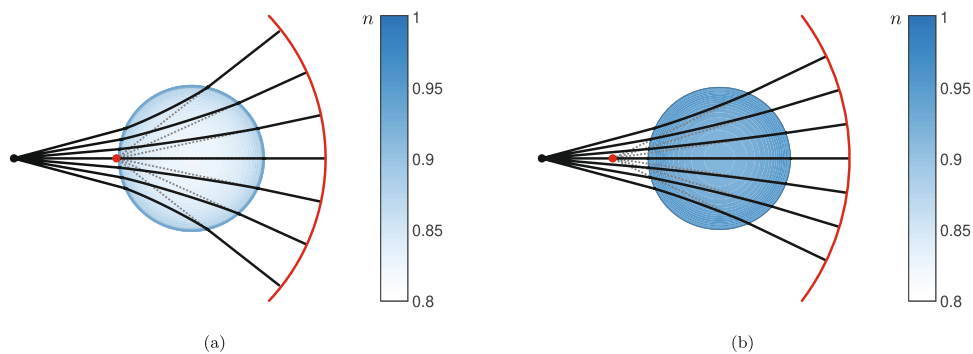

Fig. 5 Virtual image lenses with a source farther from the lens than the image. A ray-tracing representation is provided in the case $r_s > r_i$, leading to a solution with a refractive index below 1. Actual rays are in solid lines while virtual rays are in dotted lines. Two source positions, represented by a black dot, are illustrated: (**a**) $r_i = 1$ and (**b**) $r_i = 1.5$, with $r_s = 2.5$ and $M = 0$ in both cases, where M is a parameter proportional to the total change of polar angle as the ray propagates from the source to the image. Here, the source, the image and the center of the lens are aligned. The virtual image is illustrated with a red dot and the corresponding wavefront is represented with a red arc. All rays are represented with the same electrical length, with the end of the rays marking an equiphase front, in agreement with the expected wavefront.

Fig. 4d). A ray-tracing representation is also provided for inhomogeneous lenses with $r_s > r_i \geq 1$, thus leading to refractive index values below 1. Two configurations are illustrated in Fig. 5 for $r_i = 1$ and $r_i = 1.5$, with $r_s = 2.5$ in both cases. The refractive index profiles are essentially symmetric to those obtained with $r_s < r_i$, having here the lower values at the center of the lens. Similarly to the case with refractive index above 1, moving the virtual image away from the lens and towards the real source reduces the refractive index variation across the lens, converging toward an invisible lens in the particular case where $r_i = r_s$.

All the results discussed above are obtained for $M = 0$. The general solution is also validated with $M > 0$, corresponding to a generalization of the problem equivalent to the one proposed by

Eaton[9]. The ray-tracing representations reported in Fig. 6 are obtained with $r_i = 2$ and $M = 0.8$. In Fig. 6a, the source is on the surface of the lens, while in Fig. 6b, the source is at infinity. A ray-tracing representation in the equivalent geodesic lens is provided in Fig. 6c and 6d for the configurations in Fig. 6a and 6b, respectively. The proposed complementary problem leads to the retro-reflective Eaton lens for $r_s = -\infty$, $r_i = +\infty$ and $M = 1$.

The configurations illustrated in Fig. 6 have a very high refractive index at the center of the lens. This may be significantly reduced using a half-lens design combined with a planar mirror. The concept of half-Luneburg lenses was introduced in the early 1950's to reduce the size and weight of Luneburg lenses[47]. With the addition of a planar mirror passing through the center of the
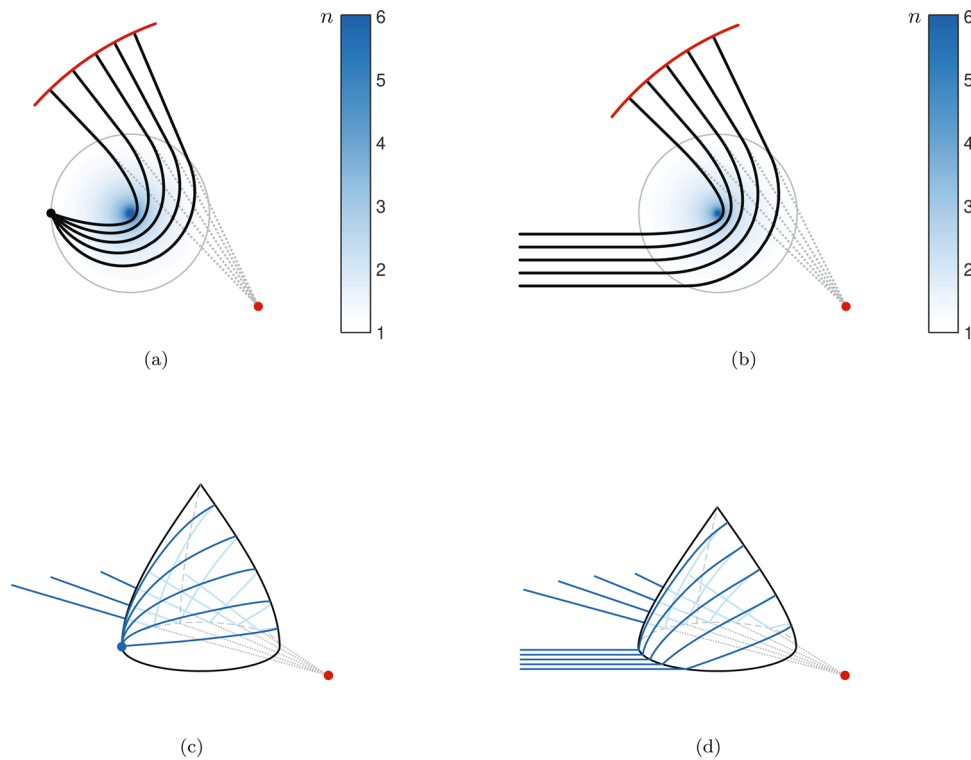
Fig. 6 Virtual image lenses with the source and image not aligned with the center of the lens. A ray-tracing representation is provided in the case $M > 0$, where M is a parameter proportional to the total change of polar angle as the ray propagates from the source to the image. Actual rays are in solid lines while virtual rays are in dotted lines. **a**, **b** Inhomogeneous and (**c**, **d**) geodesic lenses are compared for two source positions: (**a**, **c**) $r_s = 1$, corresponding to a source on the surface of the lens, and (**b**, **d**) $r_s = -\infty$, corresponding to an incident plane wave with parallel incoming rays. In both cases, $r_i = 2$ and $M = 0.8$. All dimensions are normalized to the lens radius. The point source and emerging rays are illustrated in black in the case of inhomogeneous lenses and in blue in the case of geodesic lenses. In these particular cases, the rays are wrapping around on the geodesic lenses, with rays passing behind the visible surface represented in lighter blue. The virtual image is represented in both cases with a red dot. The expected wavefront is illustrated with a red arc in the case of the inhomogeneous lenses. All rays are represented with the same electrical length, with the end of the rays marking an equiphase front, in agreement with the expected wavefront.

lens, the focusing properties are preserved and the source is transformed into a virtual source, still focusing the rays at infinity but in a symmetric direction with respect to the plane of the mirror. This property is also maintained in the case of planar[48] and geodesic[49] half-Luneburg lenses. This solution reduces the size of the lens by a factor of two, albeit with a reduced scanning range, as the omni-directional characteristic of the original Luneburg lens is lost. This solution may be of interest in some specific applications with limited field of view. This concept is also applicable to the virtual image lens introduced here. A ray-tracing representation of an inhomogeneous half-lens design is provided in Fig. 7. The lens is also designed with $r_i = 2$, for comparison with the lens reported in Fig. 6a. The singularity is removed and the maximum for the refractive index is around 1.2.

Full-wave results. To validate further the theory, a full-wave model has been implemented in the frequency domain using the EM solver Ansys HFSS. The model is a geodesic lens in a parallel plate waveguide configuration with a homogeneous medium having a refractive index of 1. This modeling approach has already proved to be accurate for the characterization of geodesic lenses in the microwave domain[39,40,49]. A representation of the electric field distribution is provided in Fig. 8 for a virtual lens with parameters $r_s = 1$, $r_i = 2.5$ and $M = 0$, corresponding to the case illustrated in Fig. 4a, c. Numerical results are reported at 10, 20 and 30 GHz with a lens of 100 mm in diameter. The lens is excited with an isotropic source. These results confirm the frequency-independent response of the structure. The cylindrical
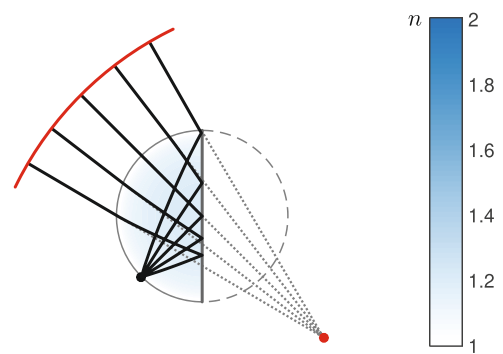

Fig. 7 Virtual image half-lens combined with a planar mirror. A ray-tracing representation is provided in the case of an inhomogeneous half-lens with a planar mirror cutting through the middle of the lens. Actual rays are in solid lines while virtual rays are in dotted lines. The missing half-lens is schematically represented with a dashed line and no refractive index distribution. The case provided corresponds to a source on the surface of the lens, $r_s = 1$, and design parameters $r_i = 2$ and $M = 0$, where M is a parameter proportional to the total change of polar angle as the ray propagates from the source to the image. Here, the source, the mirrored image and the center of the lens are aligned. The point source and emerging rays are illustrated in black and the virtual image is represented with a red dot. The expected wavefront is illustrated with a red arc. All rays are represented with the same electrical length, with the end of the rays marking an equiphase front, in agreement with the expected wavefront.
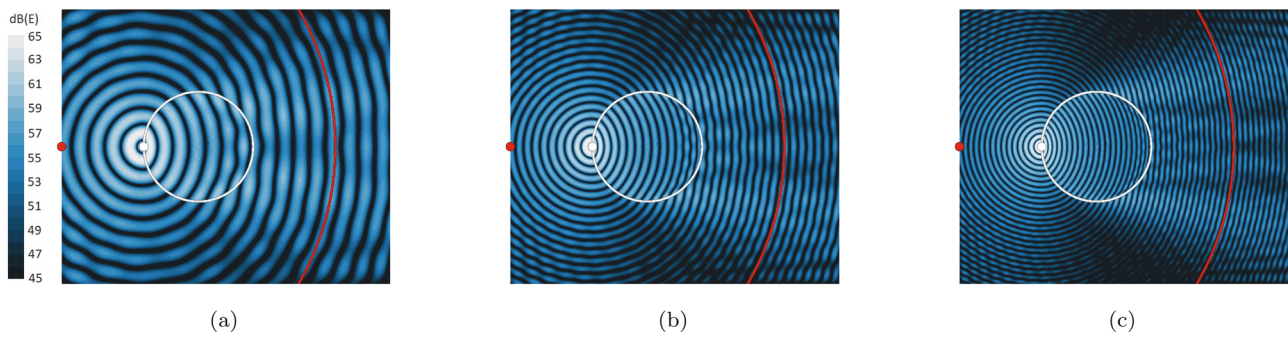
Fig. 8 Full-wave simulation results of a virtual image lens. The analyzed geodesic lens has a diameter of 100 mm and design parameters $r_s = 1$, $r_i = 2.5$ and $M = 0$, where r_s and r_i are the radial positions of the source and the image, respectively, and M is a parameter proportional to the total change of polar angle as the ray propagates from the source to the image. Numerical results are reported at (**a**) 10 GHz, (**b**) 20 GHz and (**c**) 30 GHz. The lens is delimited by a white circle and the point source is represented by a white dot. The virtual image is illustrated as a red dot and the corresponding theoretical wavefront is represented as a red arc, showing good agreement with the equiphase lines produced on the right side of the lens at all analyzed frequencies.
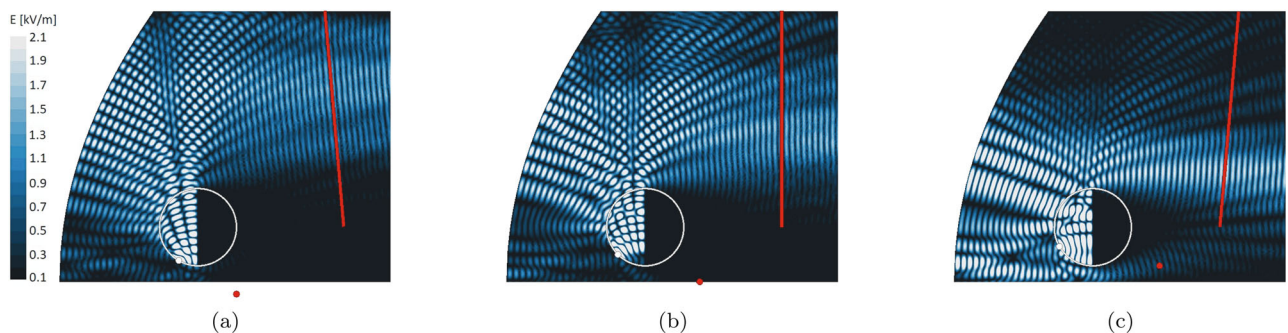

Fig. 9 Full-wave simulation results of a dual-optics system based on a virtual image half-lens. The analyzed geodesic half-lens has a diameter of 100 mm and design parameters $r_s = 1$, $r_i = 2$ and $M = 0$, where r_s and r_i are the radial positions of the source and the image, respectively, and M is a parameter proportional to the total change of polar angle as the ray propagates from the source to the image. The offset parabolic reflector has a focal length of 250 mm. Numerical results are reported at 20 GHz for a virtual source angular position (**a**) $\phi = -60°$, (**b**) $\phi = -45°$ and (**c**) $\phi = -20°$, where ϕ is the polar angle defined with respect to the horizontal axis passing through the center of the lens. The dual-optics geometry is set to collocate the focal point of the parabolic reflector with the virtual source at $\phi = -45°$. The lens is delimited by a white circle and the reflector is formed using the boundary condition on the left side of the analyzed space. The real source is represented with a white dot, while the virtual source is illustrated with a red dot. The expected wavefront is represented with a red line, showing good agreement with the equiphase lines produced on the right side of the dual-optics system for all analyzed source positions.

wavefront centered on the feed is clearly visible on the left side of the plots. The virtual image and expected cylindrical wavefront are highlighted in red. Besides some residual diffraction effects, the transformed wavefront is clearly visible on the right side of the plots and fully in line with predictions. The diffraction patterns are a consequence of the numerical implementation, requiring to discretize the lens profile, and of the transition between the surrounding planar parallel plate waveguide and the geodesic lens, leading to some residual aberrations. More generally, some limitations may result from the practical implementation of the lens. Nevertheless, these numerical results confirm the focusing properties of the virtual image lens solution detailed in this paper, even in the case of an electrically small lens as the analyzed model has a diameter of about three wavelengths only at the lowest reported frequency.

As mentioned in the introduction, the proposed family of lenses can also find applications in multi-optics systems. The analogy with dual-reflector configurations indicate that virtual image lenses may be used in a Cassegrain-like reflector geometry, which is known to provide a more compact layout[42]. A planar model of a lens-fed offset parabolic reflector geometry was implemented in Ansys HFSS. The numerical results for various positions of the source are reported in Fig. 9a-c. To further reduce the size of the proposed geometry, a half-lens geometry is

implemented, corresponding to the case illustrated in Fig. 7. For these analyses, a more directive source is used to limit interference patterns coming from back radiation and to facilitate the visualization of the plane wave produced by the dual-optics system. Specifically, a rectangular waveguide with a broadwall dimension of 8.64 mm is used, corresponding to the standard size WR34 suitable for K_a-band systems. Numerical results are reported at 20 GHz. The focal length of the offset parabolic reflector is set to 250 mm, while the lens diameter remains 100 mm. Due to the offset geometry, the distance that serves as reference for the magnification effect of this dual-optics system is the distance from the focal point to the reflector surface passing through the center of the lens. The reflector geometry was defined such that this distance is approximately 300 mm, thus magnifying the properties of the lens by a factor of 3[45]. The focal point of the parabolic reflector is set to coincide with the virtual image located at $-45°$ in the coordinate frame with origin the center of the lens, corresponding to the configuration in Fig. 9b, where the virtual image is highlighted with a red dot. For sources placed at $\pm 15°$ around that nominal position, a tilt of the wavefront is observed while maintaining the plane wave characteristic. Due to the magnifying geometry, the expected tilt angle is equal to the source angular displacement divided by the magnification factor, corresponding to about $\pm 5°$. The expected wavefront is

represented in Fig. 9 with a red solid line. The numerical results are well in line with predictions. These results provide a first demonstration of the use of the proposed virtual image lens in dual-optics systems.

Conclusions

We defined a family of spherically and rotationally symmetric lenses with a virtual image as the solution to the complement of the generalized Luneburg lens problem. An analytical formulation based on the equivalence between inhomogeneous lenses and geodesic lenses was proposed and numerical results were reported, emphasizing the complementary nature of these lenses with those obtained as a solution to the generalized Luneburg lens problem. A ray-tracing model was used to illustrate the focusing properties of various lens configurations. The solution was further validated using full-wave EM modeling, both as stand-alone and as feeding structure in a dual-optics system. The numerical results confirmed the expected virtual image focusing properties.

This complementary family of lenses is expected to extend the range of existing quasi-optical and optical systems, providing advanced focusing properties through the use of multi-optics configurations. Combined with the recent developments on metamaterials and transformation optics, this is expected to foster a number of new developments in the microwave, terahertz and optical domains.

Methods

Derivation of the geodesic lens profile. Using the linearity of integration, one may decompose the function defining the geodesic lens profile, $s(\rho)$, as follows:

$$s(\rho) = s_M(\rho) + s_s(\rho) + s_i(\rho) \tag{12}$$

where

$$\int_L^1 \frac{L s'_M(\rho) \mathrm{d}\rho}{\rho \sqrt{\rho^2 - L^2}} = \frac{M\pi}{2}, \tag{13}$$

and the other two terms correspond to the same equation replacing the right-hand side of the equation by $\frac{1}{2}\arcsin(L/r_s)$ and $\frac{1}{2}\arcsin(L/r_i)$ for $s_s(\rho)$ and $s_i(\rho)$, respectively.

Introducing the change of variables $u = 1/\rho^2$ and $x = 1/L^2$, Eq. (13) can be rewritten as follows:

$$\int_1^x \frac{u s'(u) \mathrm{d}u}{\sqrt{x - u}} = -\frac{M\pi}{2} = f(x), \tag{14}$$

where $s'_M(u) = \mathrm{d}s_M/\mathrm{d}u$ is the unknown. This takes the form of an Abel integral equation and has the following solution:

$$x\, s'_M(x) = \frac{1}{\pi}\left(\frac{f(1)}{\sqrt{x-1}} + \int_1^x \frac{f'(t)\mathrm{d}t}{\sqrt{x-t}}\right). \tag{15}$$

In this case, the function $f(x)$ is constant, which simplifies greatly the evaluation and

$$s'_M(x) = -\frac{M}{2x\sqrt{x-1}}, \tag{16}$$

which may be rewritten as

$$s'_M(L) = \frac{M}{\sqrt{1-L^2}}. \tag{17}$$

This leads to the solution:

$$s_M(L) = M \arcsin L, \tag{18}$$

with the corresponding term reported in Eq. (10). The remaining terms, $s_s(\rho)$ and $s_i(\rho)$, are derived using a similar approach, which is not detailed here as these terms can also be found by analogy with the derivation reported in[19].

Data availability

The numerical data that support the findings of this study are available from the corresponding authors upon reasonable request.

References

1. Maxwell, J. C. Problems (3). *Camb. Dublin Math. J.* **8**, 188 (1853).
2. Maxwell, J. C. Solutions of problems (prob. 3, vol. viii. p. 188). *Camb. Dublin Math. J.* **9**, 9–11 (1854).
3. Born, M. & Wolf, E. *Principles of Optics* (Cambridge University of Press,1989).
4. Miñano, J. C. Perfect imaging in a homogeneous three-dimensional region. *Opt. Express* **14**, 9627–9635 (2006).
5. Tyc, T., Herzánová, L., Šarbort, M. & Bering, K. Absolute instruments and perfect imaging in geometrical optics. *N. J. Phys.* **13**, 115004 (2011).
6. Tyc, T. & Danner, A. J. Absolute optical instruments, classical superintegrability, and separability of the Hamilton-Jacobi equation. *Phys. Rev. A* **96**, 053838 (2017).
7. Niven, W. D. *The Scientific Papers of James Clerk Maxwell* (Dover Publications, Inc. 9, 76–79 (1890).
8. Luneburg, R. K. *Mathematical Theory of Optics* (Spenser Lens Co.,1944).
9. Eaton, J. E. On spherically symmetric lenses. *Trans. IRE Professional Group Antennas Propag.* **PGAP-4**, 66–71 (1952).
10. Gutman, A. S. Modified Luneburg lens. *J. Appl. Phys.* **25**, 855–859 (1954).
11. Morgan, S. P. General solution of the Luneberg lens problem. *J. Appl. Phys.* **29**, 1358–1368 (1958).
12. Colombini, E. Index-profile computation for the generalized Luneburg lens. *J. Optical Soc. Am.* **71**, 1403–1405 (1981).
13. Sochacki, J. Generalized Luneburg lens problem. an analytical solution and its simplifications. *Opt. Applicata* **13**, 487–495 (1983).
14. Rinehart, R. F. A solution of the problem of rapid scanning for radar antennae. *J. Appl. Phys.* **19**, 860–862 (1948).
15. Rinehart, R. F. A family of designs for rapid scanning radar antennas. *Proc. IRE* **40**, 686–688 (1952).
16. Leonhardt, U. Optical conformal mapping. *Sci. Rep.* **312**, 1777–1780 (2006).
17. Pendry, J. B., Schurig, D. & Smith, D. R. Controlling electromagnetic fields. *Sci. Rep.* **312**, 1780–1782 (2006).
18. Kunz, K. S. Propagation of microwaves between a parallel pair of doubly curved conducting surfaces. *J. Appl. Phys.* **25**, 642–653 (1954).
19. Šarbort, M. & Tyc, T. Spherical media and geodesic lenses in geometrical optics. *J. Opt.* **14**, 11 (2012).
20. Tyc, T. Magnifying absolute instruments for optically homogeneous regions. *Phys. Rev. A* **84**, 03180(R)(2011).
21. Hendi, A., Henn, J. & Leonhardt, U. Ambiguities in the scattering tomography for central potentials. *Phys. Rev. Lett.* 97, 073902 (2006).
22. Tyc, T., Chen, H., Danner, A. & Xu, Y. Invisible lenses with positive isotropic refractive index. Phys. Rev. A 90, 053829 (2014).
23. Cornbleet, S. & Rinous, P. J. Generalised formulas for equivalent geodesic and nonuniform refractive lenses. *IEE Proc.* **128, Pt. H**, 95–101 (1981).
24. Hollis, J. S. & Long, M. W. A Luneberg lens scanning system. *IRE Trans. Antennas Propag.* **AP-5**, 21–25 (1957).
25. Johnson, R. C. The geodesic Luneburg lens. *Microwave J.* **5**, 76–85 (1962).
26. Kundtz, N. & Smith, D. R. Extreme-angle broadband metamaterial lens. *Nat. Mater.* **9**, 129–132 (2010).
27. Pfeiffer, C. & Grbic, A. A printed, broadband Luneburg lens antenna. *IEEE Trans. Antennas Propag.* **58**, 3055–3059 (2010).
28. Ma, H. F. & Cui, T. J. Three-dimensional broadband and broad-angle transformation-optics lens. *Nat. Commun.* **1**, 1–7 (2010).
29. Su, Y. & Chen, Z. N. A flat dual-polarized transformation-optics beamscanning Luneburg lens antenna using PCB-stacked gradient index metamaterials. *IEEE Trans. Antennas Propag.* **66**, 5088–5097 (2018).
30. Zetterstrom, O., Hamarneh, R. & Quevedo-Teruel, O. Experimental validation of a metasurface luneburg lens antenna implemented with glide-symmetric substrate-integrated-holes. *IEEE Antennas Wirel. Propag. Lett.* **20**, 698–702 (2021).
31. Numan, A. B., Frigon, J.-F. & Laurin, J.-J. Printed W-band multibeam antenna with Luneburg lens-based beamforming network. *IEEE Trans. Antennas Propag.* **66**, 5614–5619 (2018).
32. Abbasi, M. A. B. & Fusco, V. F. Maxwell fisheye lens based retrodirective array. *Nat. Sci. Rep.* **9**, 1–8 (2019).
33. Headland, D., Withayachumnankul, W., Yamada, R., Fujita, M. & Nagatsuma, T. Terahertz multi-beam antenna using photonic crystal waveguide and Luneburg lens. *APL Photonics* **3**, 1–18 (2018).
34. Amarasinghe, Y., Mittleman, D. M. & Mendis, R. A Luneburg lens for the terahertz region. *J. Infrared, Millim., Terahertz Waves* **40**, 1129–1136 (2019).
35. Arigong, B. et al. Design of wide-angle broadband Luneburg lens based optical couplers for plasmonic slot nano-waveguides. *J. Appl. Phys.* **114**, 1–5 (2013).
36. Zhao, Y.-Y. et al. Three-dimensional Luneburg lens at optical frequencies. *Laser Photonics Rev.* **10**, 665–672 (2016).
37. Quevedo-Teruel, O. et al. Glide-symmetric fully metallic Luneburg lens for 5G communications at Ka-band. *IEEE Antennas Wirel. Propag. Lett.* **17**, 1588–1592 (2018).
38. Xue, L. & Fusco, V. 24 GHz automotive radar planar Luneburg lens. *IET Microw., Antennas Propag.* **1**, 624–628 (2007).

39. Liao, Q., Fonseca, N. J. G. & Quevedo-Teruel, O. Compact multibeam fully metallic geodesic Luneburg lens antenna based on non-euclidean transformation optics. *IEEE Trans. Antennas Propag.* **66**, 7383–7388 (2018).

40. Fonseca, N. J. G., Liao, Q. & Quevedo-Teruel, O. Equivalent planar lens ray-tracing model to design modulated geodesic lenses using non-euclidean transformation optics. *IEEE Trans. Antennas Propag.* **68**, 3410–3422 (2020).

41. Fonseca, N. J. G. The water drop lens: revisiting the past to shape the future. *EurAAP Rev. Electromagn* in Press.

42. Rusch, W. V. T., Prata, A., Rahmat-Samii, Y. & Shore, R. A. Derivation and application of the equivalent paraboloid for classical offset Cassegrain and Gregorian antennas. *IEEE Trans. Antennas Propag.* **38**, 1141–1149 (1990).

43. Lima, E. B., Matos, S. A., Costa, J. R., Fernandes, C. A. & Fonseca, N. J. G. Circular polarization wide-angle beam steering at Ka-band by in-plane translation of a plate lens antenna. *IEEE Trans. Antennas Propag.* **63**, 5443–5455 (2015).

44. Mimouni, S. Lentille a immersion solide a capacite de focalisation accrue. French Patent 2 899 343 (2006).

45. Fonseca, N. J. G., Girard, E. & Legay, H. Doubly curved reflector design for hybrid array fed reflector antennas. *IEEE Trans. Antennas Propag.* **66**, 2079–2083 (2018).

46. Mitchell-Thomas, R. C. et al. Lenses on curved surfaces. *Opt. Lett.* **39**, 3551–3554 (2014).

47. Peeler, G., Kelleher, K. & Coleman, H. Virtual source Luneberg lenses. *Trans. IRE Professional Group Antennas Propag.* **2**, 94–99 (1954).

48. Lu, H., Liu, Z., Liu, Y., Ni, H. & Lv, X. Compact air-filled Luneburg lens antennas based on almost-parallel plate waveguide loaded with equal-sized metallic posts. *IEEE Trans. Antennas Propag.* **67**, 6829–6838 (2019).

49. Fonseca, N., Liao, Q. & Quevedo–Teruel, O. Compact parallel–plate waveguide half–Luneburg geodesic lens in the Ka–band. *IET Microw. Antennas Propag.* **15**, 123–130 (2021).

Acknowledgements

Author contributions

N.F. conceived the original idea, N.F., T.T. and O.Q.-T. contributed to formulate the solution, T.T. and N.F. developed the analytical and numerical models, N.F. prepared the manuscript, N.F., T.T. and O.Q.-T. contributed to the review and editing.

Competing interests

The authors declare no competing interests.

Additional information

Correspondence and requests for materials should be addressed to Nelson J. G. Fonseca.

Peer review information *Communications Physics* thanks the anonymous reviewers for their contribution to the peer review of this work.

Reprints and permission information is available at http://www.nature.com/reprints

Publisher's note Springer Nature remains neutral with regard to jurisdictional claims in published maps and institutional affiliations.